Materials Today Communications 31 (2022) 103771

Contents lists available at ScienceDirect

Materials Today Communications

journal homepage: www.elsevier.com/locate/mtcomm

Microstructure and hot deformation behavior of the Cu-1Ni-0.9Sn-0.5Ti-0.3Cr alloy

Shunlong Tang [a], Meng Zhou [a,b,c,*], Xu Li [d], Yi Zhang [a,b,c,*], Deye Xu [a], Zhiyang Zhang [a], Baohong Tian [a,b,c], Yanlin Jia [e], Yong Liu [a,b,c], Alex A. Volinsky [f,g], Ekaterina S. Marchenko [g]

[a] School of Materials Science and Engineering, Henan University of Science and Technology, Luoyang 471023, PR China
[b] Provincial and Ministerial Co-construction of Collaborative Innovation Center for Non-ferrous Metals New Materials and Advanced Processing Technology, Luoyang 471023, Henan, PR China
[c] Henan Province Key Laboratory of Nonferrous Materials Science and Processing Technology, Luoyang 471023, PR China
[d] Center for Advanced Measurement Science, National Institute of Metrology, Beijing 100029, PR China
[e] College of Materials Science and Engineering, Central South University, Changsha 410083, PR China
[f] Department of Mechanical Engineering, University of South Florida, 4202 E. Fowler Ave. ENG 030, Tampa 33620, USA
[g] National Research Tomsk State University, Laboratory of Superelastic Biointerfaces, 36 Lenin Ave., Tomsk 634050, Russia

ARTICLE INFO

Keywords:
Cu-1Ni-0.9Sn-0.5Ti-0.3Cr alloy
Hot deformation behavior
Constitutive equation
Processing map
Microstructure evolution

ABSTRACT

The Cu-1Ni-0.9Sn-0.5Ti-0.3Cr alloy was prepared by vacuum induction melting. The hot deformation experiments with the alloy were carried out using the Gleeble-1500 deformation simulation device at 0.001–10 s^{-1} strain rate, and 500–900 °C deformation temperature. The hot working constitutive equation for the Cu-1Ni-0.9Sn-0.5Ti-0.3Cr alloy was established. The optimal hot processing of the Cu-1Ni-0.9Sn-0.5Ti-0.3Cr alloy is at 725–900 °C and 0.01–0.223 s^{-1} strain rate, so the alloy can obtain the required defect-free structure and excellent machinability. The alloy microstructure was analyzed using the electron backscatter diffraction, and the main texture of the Cu-1Ni-0.9Sn-0.5Ti-0.3Cr alloy deformed at 800 ℃ is the {011}< 100 > Goss texture, which is replaced by the {011}< 211 > brass texture at 900 °C. Recrystallization is promoted by higher deformation temperature. The recrystallization process provides energy for recrystallization by consuming dislocations, and the geometrically necessary dislocation density decreases with temperature. Transmission electron microscopy of the alloy shows that the precipitates are mainly Cu and NiTi phases. The interface between the two precipitated phases is semi-coherent. The precipitated phase at a semi-coherent interface can produce smaller elastic stress and lower interfacial energy, thus improving the refinement rate. Meanwhile, the Cu and NiTi phases have high toughness, and grain refinement can effectively improve the strength and hardness of the alloy.

1. Introduction

Copper can form alloys with many different elements. Copper alloys have better physical and mechanical properties than pure copper, so they have been widely used in electronics, and defense, as electromagnetic relays, lead frames, in communications technology, aerospace, and other fields [1–5]. At present, in order to obtain copper alloys with high strength, electrical conductivity, and excellent comprehensive properties, the commonly used method is to add trace alloying elements and rare earth elements into the copper matrix such as Ti [6], Ni [7,8], Sn [9], Cr [10], Fe [11], Mg [12], Co [13], Y [14], Ce [15] and so on. With the rapid advancement of 5 G chips and high-end lead frames, the research and development of new copper alloys are imminent. By adding Ni, Sn, Ti, and Cr elements to Cu, the precipitation-strengthened Cu-1Ni-0.9Sn-0.5Ti-0.3Cr alloy was obtained. Adding Ti to Cu can refine grains and improve alloy strength. The addition of Cr can refine the microstructure and improve the high-temperature stability of the alloy. Adding a certain amount of Sn can enhance the ability to hinder dislocation movement and improve the alloy strength. Ni forms precipitation phases with Sn and Ti elements, which cause precipitation strengthening and improve the alloy's mechanical properties. Copper and various metals are melted, annealed and solution treated to obtain a saturated solid solution alloy. Lattice distortion will occur during the formation of solid solution and hinder dislocation movement, thus strengthening the alloy. Adding alloying elements, thermal deformation or aging treatment improve the performance of copper alloys, so they

* Corresponding authors at: School of Materials Science and Engineering, Henan University of Science and Technology, Luoyang 471023, PR China.
E-mail addresses: volinsky@usf.edu (M. Zhou), mes@mail.tsu.ru (Y. Zhang).

https://doi.org/10.1016/j.mtcomm.2022.103771
Received 1 March 2022; Received in revised form 23 May 2022; Accepted 31 May 2022
Available online 3 June 2022

finally meet the performance requirements of 5 G chips and high-end lead frames.

Fu et al. [16] studied the role of solidification texture on the hot deformation behavior of the Cu-Ni-Si alloy with columnar grains. Ni_2Si precipitates in the Cu-Ni-Si alloy, along with dynamic recrystallization (DRX) increased the alloy flow stress. Zhang et al. [17] found that the Cu-Fe-Nb alloy contains nanocrystals, Nb precipitates, and iron fibers, resulting in the alloy's high strength. Yong et al. [18] studied the hot deformation behavior of the CuAlMn shape memory alloy and found that the α phase was the main factor affecting the alloy's thermal deformation behavior. Liu et al. [19] studied hot deformation and microstructure evolution of Cu-Ni-Co-Si alloys and found that the precipitated $(Ni,Co)_2Si$ phase hindered dislocations movement, increasing the alloy strength. Liu et al. [20] investigated the effects of cold rolling on the Cu-3Ti-3Ni-0.5Si alloy hardening by aging. The main precipitated phase in the Cu-3Ti-3Ni-0.5Si alloy was Ni_3Ti, but with the increased deformation, the stripe-like morphology of the Ni_3Ti phase changed to spherical morphology. Yu et al. [21] designed the Cu-Ni-Sn-Si alloy by using the cluster plus gel atom model. The introduction of silicon into the Cu-Ni-Sn alloy results in the disappearance of the layered structure formed in the as-cast alloy, and the introduction of silicon also inhibits the discontinuous precipitation during aging. Wu et al. [22] investigated the effects of composition on aging behavior and properties of the Cu-Ni-Si-Cr alloy. It was found that the mechanical properties and precipitation degree could be improved simultaneously by the nominal concentration or effective concentration of precipitates. Stavroulakis et al. [23] found that the duration of aging treatment had a more obvious effect on the yield strength compared with the ultimate tensile strength, which indicated that the Cu-Ni-Si alloy had a softening trend with improved strain hardening potential. Zhao et al. [24] studied the microstructure and physical properties of the Cu-Ni-Si-Co-Cr alloy with high strength and high electrical conductivity and found that Co addition can promote the precipitation of Ni, Si, and Cr solute elements from the matrix, and effectively improve the electrical conductivity of the alloy. Yi et al. [25] investigated the precipitation behavior of the Cu-3.0Ni-0.72Si alloy, found a new orientation relationship between precipitates and copper matrix, and proposed the coarsening mechanism of metastable precipitates. Wang et al. [26] studied the microstructure and properties of the Cu-Ti-Sn alloy and found that Sn formed the $CuSn_3Ti_5$ phase in the copper matrix, which reduced the content of solute titanium in the copper matrix and thus improved the alloy's electrical conductivity. Liu et al. [27] investigated the thermal deformation and dynamic recrystallization behavior of Cu-3Ti-3Ni-0.5Si and found that the precipitated Ni_3Ti phase promoted dynamic recrystallization nucleation and formed stable deformation domains.

There are many studies on the aging behavior of Cu-Ti-Ni, Cu-Ni-Sn, and Cu-Ni-Si-Cr alloys, but there are few studies on the hot deformation behavior of the Cu-Ni-Sn-Ti-Cr alloys. In this paper, the precipitation-strengthened Cu-1Ni-0.9Sn-0.5Ti-0.3Cr alloy was obtained by adding Ni, Sn, Ti, and Cr elements to Cu. The thermal deformation behavior of the Cu-1Ni-0.9Sn-0.5Ti-0.3Cr alloy was investigated by hot compression tests at 500–900 °C and 0.001–10 s^{-1} strain rates using a Geeble-1500 deformation simulator.

2. Materials and methods

Standard electrolytic copper (99% pure), Cu-33%Ti intermediate alloy, pure Ni, pure Sn, and pure Cr were melted in the ZG-0.01 vacuum frequency induction furnace. After melting the alloy was poured into the sand mold with an inner diameter of 90 mm, a height of 190 mm, and an outer diameter of 170 mm, and cooled to room temperature, so the Cu-1Ni-0.9Sn-0.5Ti-0.3Cr alloy ingot used in this experiment was obtained. In the alloy smelting process, Ar was used as a protective gas to prevent the alloy's oxidation and maintain its chemical composition. In addition, a small amount of deoxidizer was added to react with impurities and float on the surface to minimize the impurities in the alloy.

The nominal and actual compositions of the Cu-1Ni-0.9Sn-0.5Ti-0.3Cr alloy are listed in Table 1. After smelting, the ingot was heated to 950 °C and annealed for 4 h. Then it was processed into cylindrical thermal compression samples with Φ 8 mm × 12 mm dimensions by electrical discharge machining. To facilitate feeding the thermocouple, a Φ 1 mm × 2 mm hole was made in the middle of each sample. The samples were tested using the Gleeble-1500 deformation simulator. They were heated at a 10 °C/s heating rate. After heating to the desired temperature, the thermal compression test was conducted for 3 min. After each deformation test, the sample was immediately cooled with water to retain the high-temperature structure after thermal deformation. The process parameters of the Cu-1Ni-0.9Sn-0.5Ti-0.3Cr alloy are as follows: 55% compression, 0.001 s^{-1}, 0.01 s^{-1}, 0.1 s^{-1}, 1 s^{-1}, and 10 s^{-1} strain rates, and 500 °C, 600 °C, 700 °C, 800 °C, and 900 °C deformation temperatures.

The sample was cut along the longitudinal plane, and the microstructure of the central part of the Cu-1Ni-0.9Sn-0.5Ti-0.3Cr alloy was analyzed. Electron backscatter diffraction (EBSD) images were observed by JSM-7800 F scanning electron microscope at 20 kV accelerating voltage. The thin-sliced EBSD samples with the size of 10 mm × 10 mm × 1 mm were first mechanically polished and then electrolytically polished. The sample was placed into a solution of 50% alcohol and 50% phosphoric acid for electrolytic polishing at 5 V and 20 °C. The diameter of the sample was 3 mm and the thickness was 50 μm. The sample was thinned with Gatan 691 ion thinner and observed using a JSM-2100 F transmission electron microscope (TEM) at 200 kV accelerating voltage.

3. Results

3.1. True stress-true strain curves

Fig. 1 shows the true stress-strain curves of the Cu-1Ni-0.9Sn-0.5Ti-0.3Cr alloy. The alloy thermal deformation has three common kinds of stress-strain behavior past yield. The first is when stress increased with strain due to work-hardening. The second is the stress increase with strain up to the peak value before leveling off due to dynamic response. The third is when the stress initially increases reaching the peak value, followed by a consequent decrease and dynamic recrystallization curve flattening [28,29].

A large number of studies have shown that the variation trend of true stress-true strain curves of the alloy during hot deformation is jointly determined by the work hardening and dynamic softening mechanisms, which can be divided into dynamic recovery (DRV) and dynamic recrystallization (DRX) [4,30]. At the early stage of thermal deformation, the heating time is short and the atoms have no time to diffuse, which will produce a large number of dislocations in the alloy. The dislocations will accumulate, forming a network of dislocation entanglements, making dislocations movement difficult, and producing a rapid rise in the flow stress. As the thermal deformation continues, the activity of atoms in the alloy increases, and the dislocations motion accelerates, promoting dynamic softening. If the dynamic recovery is dominant, the dislocations in the alloy are eliminated and the dynamic softening and work hardening are balanced, so the stress does not increase with strain, and the true stress-true strain curve of the alloy is flat. If dynamic recrystallization is dominant, dislocations arrange into low-energy structures or disappear, so that dislocation density and stress begin to decrease [5,31]. As seen in Fig. 1(a), the peak flow stress of the Cu-1Ni-0.9Sn-0.5Ti-0.3Cr alloy is 26.3 MPa at 0.001 s^{-1} strain rate and

Table 1
The nominal and analyzed composition of the Cu-1Ni-0.9Sn-0.5Ti-0.3Cr alloy.

Alloy	Alloying element (wt%)				
	Ni	Sn	Ti	Cr	Cu
Cu-1Ni-0.9Sn-0.5Ti-0.3Cr	0.96	0.850	0.343	0.222	Bal.

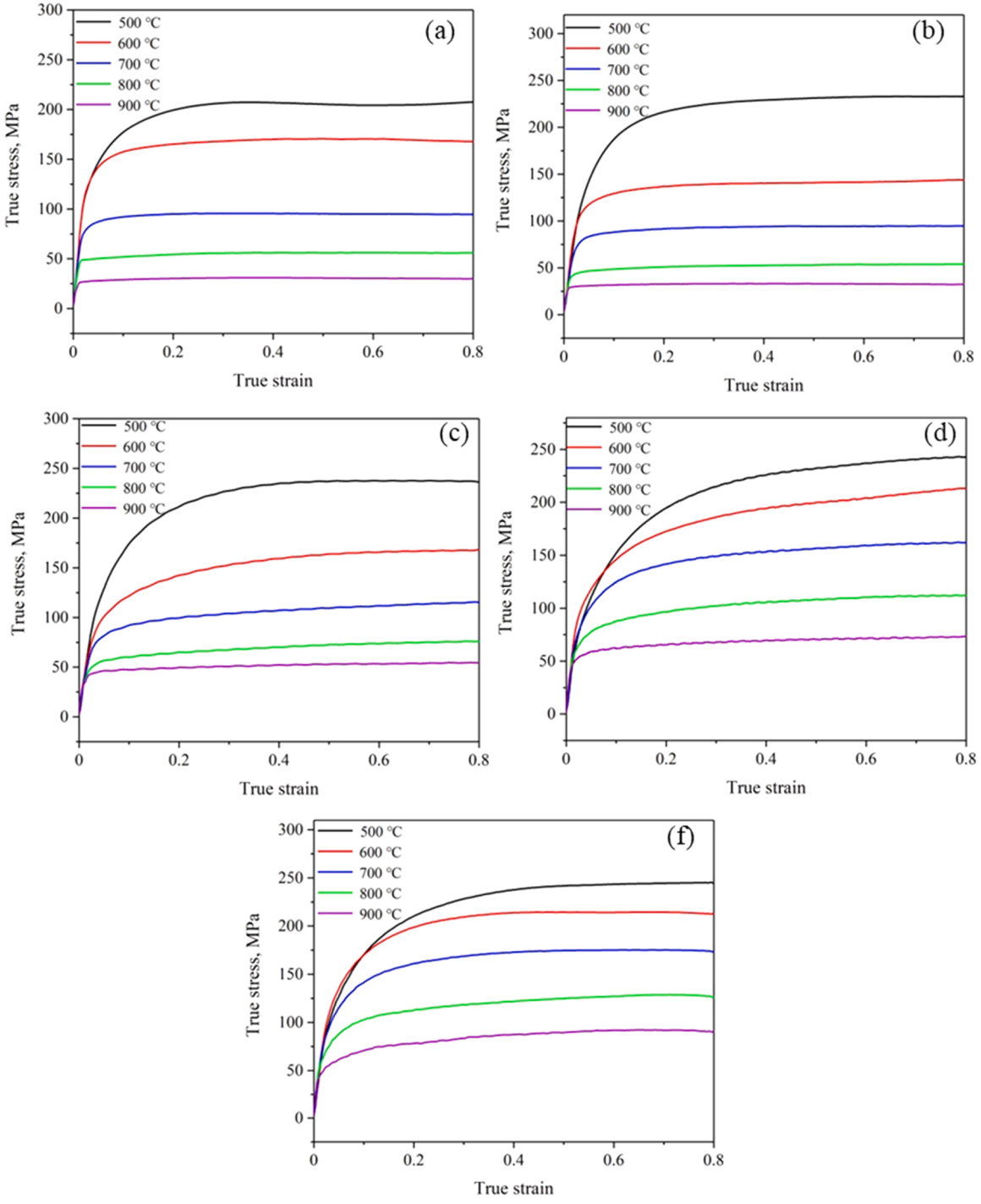

Fig. 1. True stress-strain curves of the Cu-1Ni-0.9Sn-0.5Ti-0.3Cr alloy deformed at: (a) 0.001 s^{-1}, (b) 0.01 s^{-1}, (c) 0.1 s^{-1}, (d) 1 s^{-1}, and (e) 10 s^{-1} strain rates.

900 °C deformation temperature. The peak flow stress of the Cu-1Ni-0.9Sn-0.5Ti-0.3Cr alloy increases to 80.1 MPa when the deformation temperature drops to 700 °C. When the temperature drops to 500 °C, the peak flow stress of the Cu-1Ni-0.9Sn-0.5Ti-0.3Cr alloy is 204.7 MPa, so the flow stress increased at lower deformation temperature. As seen in Fig. 1(a), (c), and (e), when the temperature is 900 °C and the strain rate is 0.001 s^{-1}, the peak value of the flow stress is 26.3 MPa. The peak stress increased to 58.7 MPa when the strain rate increased to 0.1 s^{-1}, and 94.7 MPa when the strain rate increased to 10 s^{-1}. Therefore, the flow stress increased with the strain rate.

3.2. Constitutive equation

When metals undergo plastic deformation, atoms need to cross the energy threshold before thermal motion occurs. The energy required for metal atoms to cross the threshold is called the thermal activation energy, which is important for evaluating the thermal processing of metals. In order to obtain the thermal activation energy of a metal, it is necessary to establish a suitable constitutive equation to describe the relationship between the peak stress, temperature, and strain rate during thermal deformation [32–35]. The relationship between the peak stress, strain rate, and deformation temperature in the process of thermal deformation can be established according to the hyperbolic sine model

proposed by Sellars and McTegart [36]:

$$\dot{\varepsilon} = A[\sinh(\alpha\sigma)]^n exp\left[-\frac{Q}{RT}\right] \quad (1)$$

Here, $\dot{\varepsilon}$ is the strain rate, α is the parametric constant, σ is the peak stress of the alloy, n is the parametric constant, Q is the activation energy, T is the deformation temperature in K, and R is the gas constant. Eq. (1) can be simplified into the following two different forms according to different scenarios:

$$\dot{\varepsilon} = A_1\sigma^{n1} exp\left[-\frac{Q}{RT}\right] \quad (\alpha\sigma < 0.8) \quad (2)$$

$$\dot{\varepsilon} = A_2 \exp[f(\sigma)](\beta\alpha)\exp\left[-\frac{Q}{RT}\right] \quad (\alpha\sigma > 1.2) \quad (3)$$

Taking natural logarithms of Eq. (1), (2), and (3) yields:

$$\ln\dot{\varepsilon} = n\ln[\sinh(\alpha\sigma)] - \frac{Q}{RT} + \ln A \quad (4)$$

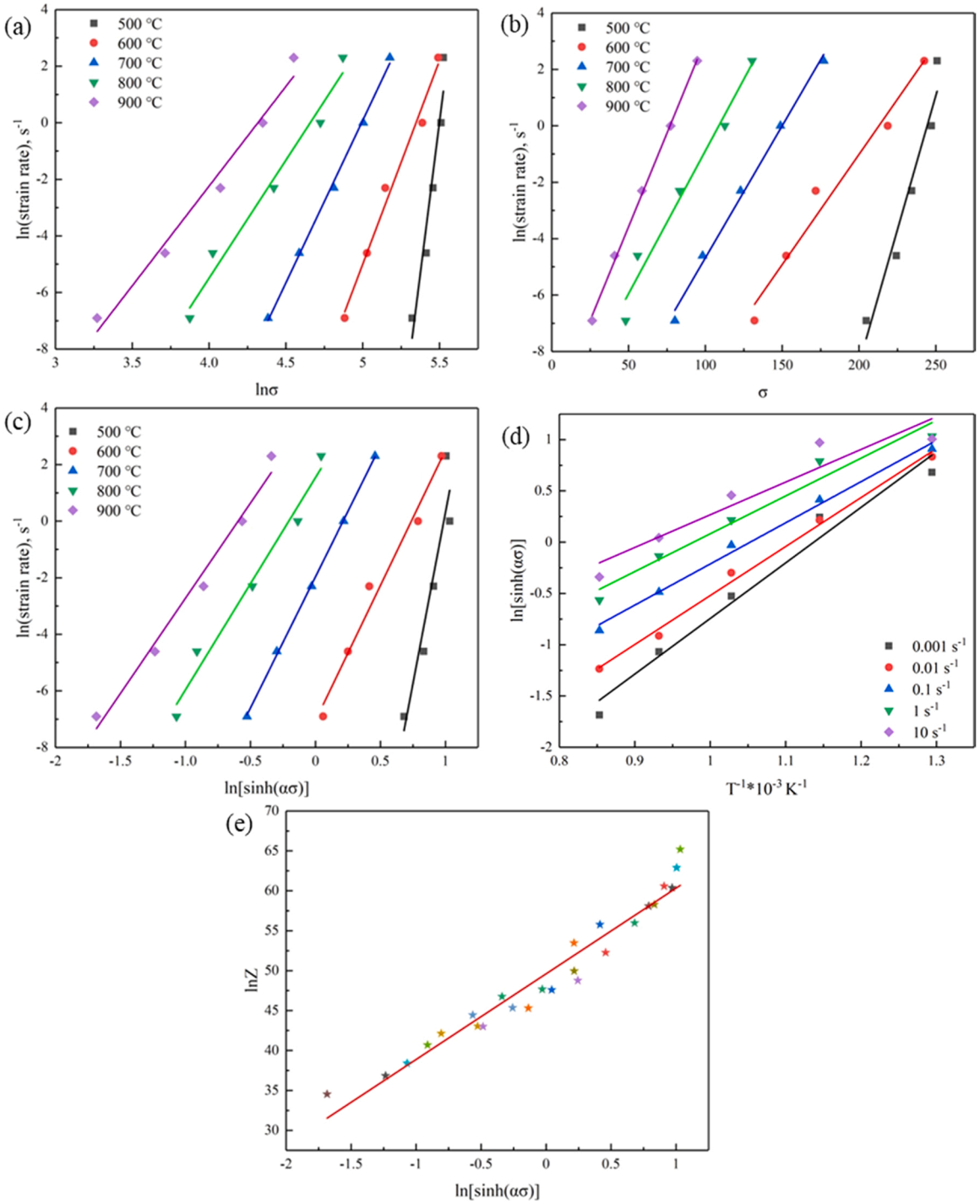

Fig. 2. The relationship between the peak stress, strain rate and temperature of the Cu-1Ni-0.9Sn-0.5Ti-0.3Cr alloy: (a) ln(strain rate)-lnσ; (b) ln(strain rate)-σ; (c) ln(strain rate)-ln[sinh(ασ)]; (d) ln[sinh(ασ)]-$T^{-1}/10^{-3}$ K^{-1}; (e) lnZ-ln[sinh(ασ)].

$$ln\dot{\varepsilon} = n_1 ln\sigma + lnA_1 - \frac{Q}{RT} \tag{5}$$

$$ln\dot{\varepsilon} = \beta\sigma + lnA_2 - \frac{Q}{RT} \tag{6}$$

The partial derivative of Eq. (1) can be obtained as:

$$Q = R\left[\frac{\partial(ln\dot{\varepsilon})}{\partial ln[\sin f_0(\alpha\sigma)]}\right]_T \left[\frac{\partial ln[\sinh(\alpha\sigma)]}{\partial(1/T)}\right]_{\dot{\varepsilon}} = RnS \tag{7}$$

The Z parameter has the following relationship with stress, temperature, and activation energy [37,38]:

$$Z = \dot{\varepsilon} exp\left[\frac{Q}{RT}\right] \tag{8}$$

By substituting Eq. (8) into Eq. (1) to find the derivative, the following relation can be obtained:

$$lnZ = lnA + nln[\sinh(\alpha\sigma)] \tag{9}$$

Here, the Z value is the self-diffusion activation energy of the lattice formed by dislocation slippage and climbing in kJ/mol. $\alpha = \beta/n$, α, β, n, A, A_1, A_2, n_1, and S are all parametric constants. The n_1, β, n, and S represent the average values of slopes corresponding to Fig. 2(a-d), respectively. $n_1 = 17.126$, $\beta = 0.121$, $\alpha = \beta/n_1 = 0.0071$, $n = 11.574$, S = 4.2, so $Q = RnS = 404.15$kJ/mol, ln$A$ is the intercept in Fig. 2(e), ln$A = 49.596$. Thus, one can calculate $A = e^{49.596}$. According to the above data, the constitutive equation of the Cu-1Ni-0.9Sn-0.5Ti-0.3Cr alloy is:

$$\dot{\varepsilon} = e^{49.596}[\sinh(0.0071\sigma)]^{11.574} exp\left[-\frac{404150}{8.314T}\right] \tag{10}$$

The activation energy of Cu is 203.6 kJ/mol [39]. The activation energy of the Cu-1Ni-0.9Sn-0.5Ti-0.3Cr alloy is 404.15 kJ/mol. There are more precipitated phases in the alloy, and the precipitated phases exist in the matrix and grain boundaries to inhibit dislocation movement so that the deformation resistance of the alloy is enhanced and the alloy has higher activation energy.

3.3. Processing maps

Processing maps are widely used to determine the optimal thermal working region of alloys [40–42]. Based on the dynamic material model (DMM), the processing map is the superimposition of the power dissipation and instability diagrams [43,44]. In the DMM model, the energy consumed in the deformation process P can be divided into two parts, G and J. G represents the power consumption related to plastic deformation, and J represents the power consumption related to microstructure change. The relationship between P, G, and J is expressed as [45]:

$$P = \sigma\dot{\varepsilon} = G + J = \int_0^{\dot{\varepsilon}} \sigma d\dot{\varepsilon} + \int_0^{\sigma} \varepsilon d\sigma \tag{11}$$

Here, $\dot{\varepsilon}$ is the strain rate in s^{-1}, and σ is the flow stress in N/m^2.

It is assumed that the material is ideal, and the linear dissipation is the ideal linear dissipation, that is, the flow stress has a linear relationship with the strain rate, at which point the theoretical dissipation quantity reaches the maximum value J_{max}:

$$J_{max} = \frac{1}{2}\sigma\dot{\varepsilon} = \frac{1}{2}P \tag{12}$$

Power dissipation efficiency η is the proportion of the dissipation covariance absorbed by materials during thermal processing to the theoretical maximum dissipation covariance [46], and the mathematical expression is:

$$\eta = \frac{J}{J_{max}} = \frac{2m}{m+1} \times 100\% \tag{13}$$

Here, m is the strain rate sensitive parameter, which can determine the amount of energy used in organizational evolution:

$$m = \frac{dJ}{dG} = \frac{\dot{\varepsilon} d\sigma}{\varepsilon d\dot{\sigma}} = \frac{d\ln\sigma}{d\ln\dot{\varepsilon}} \tag{14}$$

The energy dissipation diagram is obtained by the power dissipation efficiency, the strain rate $\dot{\varepsilon}$ and temperature T. The greater the η, the better the deformation performance of the materials. The energy dissipation diagram shows the regions with the highest η. In addition, the rheological instability zone has a great influence on the deformation performance of the alloy, and its performance is poor in the rheological instability zone, which is prone to cracking due to dislocations concentration, so this zone should be avoided. The mathematical expression of the rheological instability criterion is [47]:

$$\xi(\dot{\varepsilon}) = \frac{\sigma\ln[m/(m+1)]}{\sigma\ln\dot{\varepsilon}} + m < 0 \tag{15}$$

The instability diagram of the alloy is obtained by the instability parameter $\xi(\dot{\varepsilon})$, the strain rate $\dot{\varepsilon}$ and the temperature T. The instability diagram is mapped to the energy dissipation diagram to obtain the thermal processing diagram.

Fig. 3 shows the hot working diagram of the Cu-1Ni-0.9Sn-0.5Ti-0.3Cr alloy under different deformation conditions. In Fig. 3(a-d), the diagonal part represents the instability region of the alloy, the contours represent the corresponding entropy during the microstructure evolution of the alloy, and the number on the contours represents the power dissipation coefficient of the alloy during thermal deformation. The larger the number, the more stable the microstructure evolution of the alloy is and the better the thermal working performance of the alloy is. In Fig. 3, A, B, C, and D areas represent the optimal processing areas of the alloy with deformation of 0.1, 0.3, 0.6, and 0.8, respectively. A is the region of 700–900 °C temperature and 0.01–0.368 s^{-1} strain rate ranges, B is the region of 725–900 °C temperature and 0.007–0.368 s^{-1} strain rate ranges, C is the region of 675–900 °C temperature and 0.008–0.223 s^{-1} strain rate ranges, and D is the region of 675–900 °C temperature and 0.008–0.368 s^{-1} strain rate ranges. Combined regions A, B, C, and D indicate that the deformation has little effect on the optimal hot working properties of the Cu-1Ni-0.9Sn-0.5Ti-0.3Cr alloy. The optimal working properties of the Cu-1Ni-0.9Sn-0.5Ti-0.3Cr alloy are in the 725–900 °C temperature and 0.01–0.223 s^{-1} strain rate ranges. Instability zones should be avoided during hot working, because zone rheology, wedge cracking, holes, and adiabatic shear bands may occur in the instability zones, which may affect the machining performance [48–50]. 725–900 °C temperature and 0.01–0.223 s^{-1} strain rate should be selected as the optimal region for the Cu-1Ni-0.9Sn-0.5Ti-0.3Cr alloy hot processing performance in order to obtain the defect-free microstructure and excellent machinability of the alloy [51–53].

4. Discussion

4.1. EBSD analysis

During electron backscatter diffraction analysis the electron beam excites the surface of the tilted sample and forms a Kikuchi band to analyze the microstructure, grain size, texture, orientation of the material, and so on [1,54]. Fig. 4(a) shows the as-cast microstructure of the Cu-1Ni-0.9Sn-0.5Ti-0.3Cr alloy. Fig. 4(a-c) show the inverse pole figure (IPF) diagrams of the Cu-1Ni-0.9Sn-0.5Ti-0.3Cr alloy deformed at 800 °C and 0.01 s^{-1}, 900 °C and 0.01 s^{-1}, 700 °C and 0.1 s^{-1}, respectively. Fig. 4(a) shows a typical dendrite structure with obvious dendrite segregation. The main reason is that the cooling rate of the alloy ingot is not uniform, the alloy has unbalanced solidification, and the solute atoms have no time to diffuse and form dendrite segregation. The microstructure of the Cu-1Ni-0.9Sn-0.5Ti-0.3Cr alloy after hot deformation is shown in Fig. 4(b-d). The alloy grains are crushed by extrusion

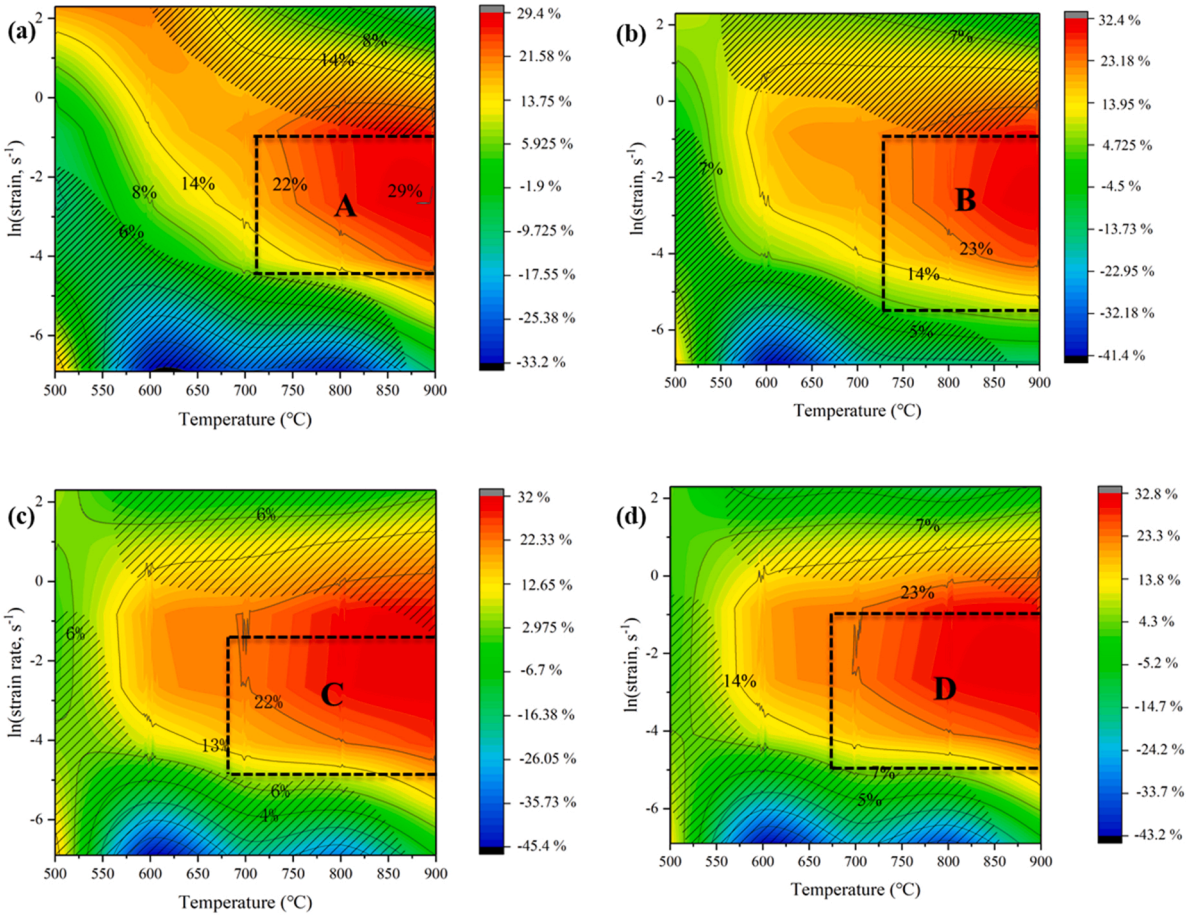

Fig. 3. Processing maps of the Cu-1Ni-0.9Sn-0.5Ti-0.3Cr alloy under different strain: (a) ε = 0.1, (b) ε = 0.3, (c) ε = 0.6, (d) ε = 0.8. The instability regions of the alloy are highlighted by oblique shadows.

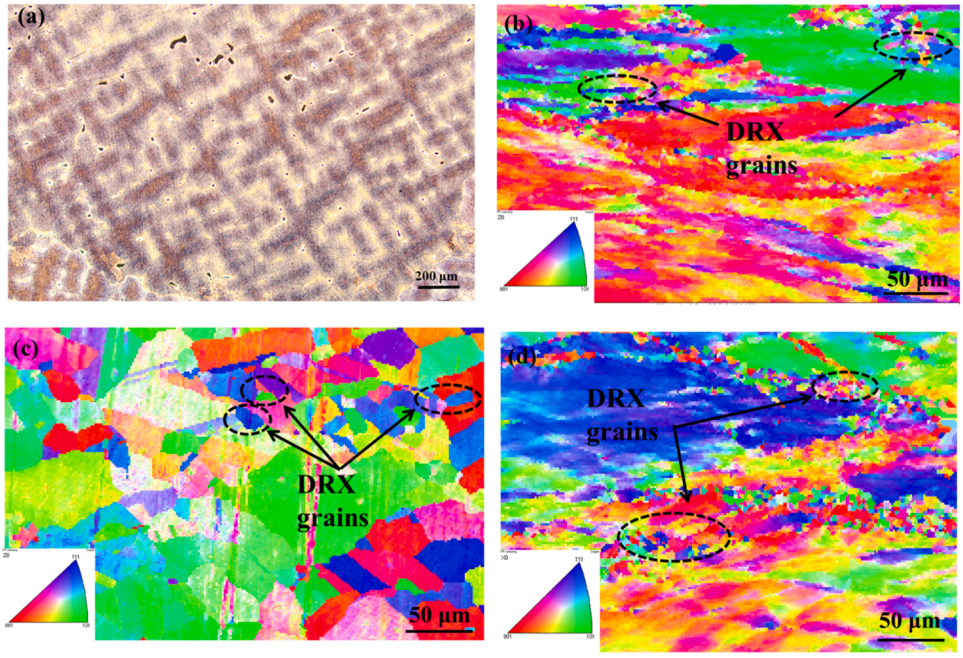

Fig. 4. (a) The as-cast microstructure of the Cu-1Ni-0.9Sn-0.5Ti-0.3Cr alloy, EBSD images of the alloy deformed at (b) 800 ℃ and 0.01 s^{-1}, (c) 900 ℃ and 0.01 s^{-1}, (d) 700 ℃ and 0.1 s^{-1}.

during hot deformation, and the grains become smaller and elongated. As seen in Fig. 4(b), (c), and (d), a certain number of recrystallized grains precipitated in the deformation grain attachment during the thermal deformation process, and these recrystallized grains and grains distributed on grain boundaries constitute a typical necklace structure [4,55]. According to Fig. 4(b) and (c), in the process of thermal deformation, with the increased deformation temperature, part of the necklace structure was replaced by recrystallized grains to form a mixed crystal structure, and the recrystallized grains also became larger, indicating that the increased deformation temperature would promote dynamic recrystallization. Compared with Fig. 4(b), the recrystallized grains in Fig. 4(d) are smaller, which is due to the lower volume fraction of recrystallized grains in the Cu-1Ni-0.9Sn-0.5Ti-0.3Cr alloy deformed at lower temperature and higher strain rate.

Fig. 5 shows the grain size distribution and misorientation angle distribution of the Cu-1Ni-0.9Sn-0.5Ti-0.3Cr alloy deformed at 800 °C and 0.01 s^{-1}, 900 °C and 0.01 s^{-1}, and 700 °C and 0.1 s^{-1}, respectively. In the process of hot deformation, with the increase in deformation temperature, dynamic recrystallization was promoted, the number of deformation grains decreased, the recrystallization grains increased, and the grain size of the alloy also grew. Compared with the grain size distribution in Fig. 5(a) and (b), the average grain size of the alloy increased from 49.8 μm to 59.9 μm with the increase in temperature from 800 °C to 900 °C, mainly because the recrystallized grains tend to grow at higher temperature and the grain size of the alloy increases with temperature. Fig. 5(d) and (e) show the values of misorientation angles of the alloy deformed at 0.01 s^{-1} strain rate and different temperatures. The average misorientation angle of the alloy at 800 °C is 9.4°. With the increase in hot deformation temperature, the alloy subgrains rotated and recrystallized grains grew, and the average misorientation angle of the alloy deformed at 900 °C increased from 9.4° to 12.6° when deformed at 800 °C. It can be seen from Fig. 5(d) and (e) that the misorientation angle of the alloy is mainly distributed at the low-angle grain boundary (LAGBs < 15°), while the large-angle grain boundary (LAGBs > 15°) is small when the misorientation angle value on both sides of grain boundary is small mainly due to the low grain boundary migration velocity. The percentage of large-angle grain boundaries increased from 16.8% to 19.9% when the deformation temperature increased from 800 °C to 900 °C at the 0.01 s^{-1} strain rate. Large angle grain boundary migration will eliminate dislocations encountered in the process of migration and leave strain-free crystals, promoting the formation of recrystallized nuclei [56]. Higher temperature also promotes the nucleation and growth of recrystallized grains, thus increasing the migration rate of grain boundaries. Therefore, the percentage of large-angle grain boundaries increased with temperature. The comparison of Fig. 5(a) and (c) shows that the average grain size of the alloy increases with the strain rate. This is because the recrystallization volume fraction of the alloy is lower at higher strain rates [27]. Compared with the alloy deformed at 800 °C and 0.01 s^{-1} in Fig. 5(d), it is shown in Fig. 5(f) that the average misorientation angle and the percentage of large-angle grain boundaries of the alloy deformed at lower hot deformation temperatures both increase. These results indicate that the volume fraction of dynamic recrystallization increases with the decrease of deformation temperature.

4.2. Texture and dislocation density changes

During the thermal deformation of the alloy, the uneven deformation degree and the different order and quantity of the slip systems movement within the grain will inevitably lead to the different texture of the alloy, and the proportion of various textures in the alloy will affect the properties of the material [57]. In order to study the texture of the alloy, it is necessary to determine the type and strength of the texture. The texture type and strength of the Cu-1Ni-0.9Sn-0.5Ti-0.3Cr alloy are specifically analyzed by drawing the pole figures and orientation density function (ODF) maps of the alloy deformed at 800 °C and 0.01 s^{-1}, 900 °C and 0.01 s^{-1}, and 700 °C and 0.1 s^{-1}, as shown in Fig. 6. There are five common recrystallization textures in copper alloys, which are the {011}< 100 > Goss texture, the {001}< 100 > cubic texture, the {111}< 211 > R texture, the {112}< 111 > copper texture, and the

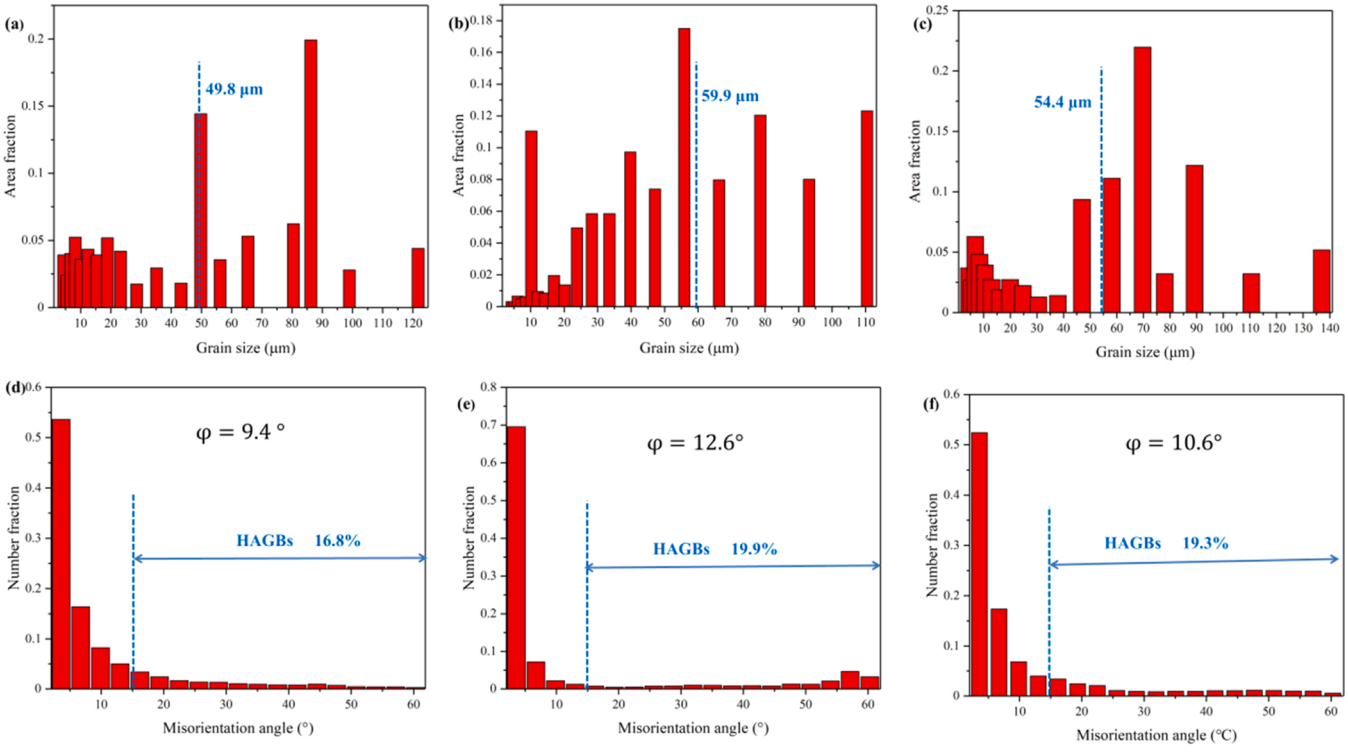

Fig. 5. Grain size distribution and EBSD misorientation angle distribution of the Cu-1Ni-0.9Sn-0.5Ti-0.3Cr alloy under different deformation conditions: (a), (d) 800 °C and 0.01 s^{-1} strain rate, (b), (e) 900 °C and 0.01 s^{-1} strain rate, (c), (f) 700 °C and 0.1 s^{-1} strain rate.

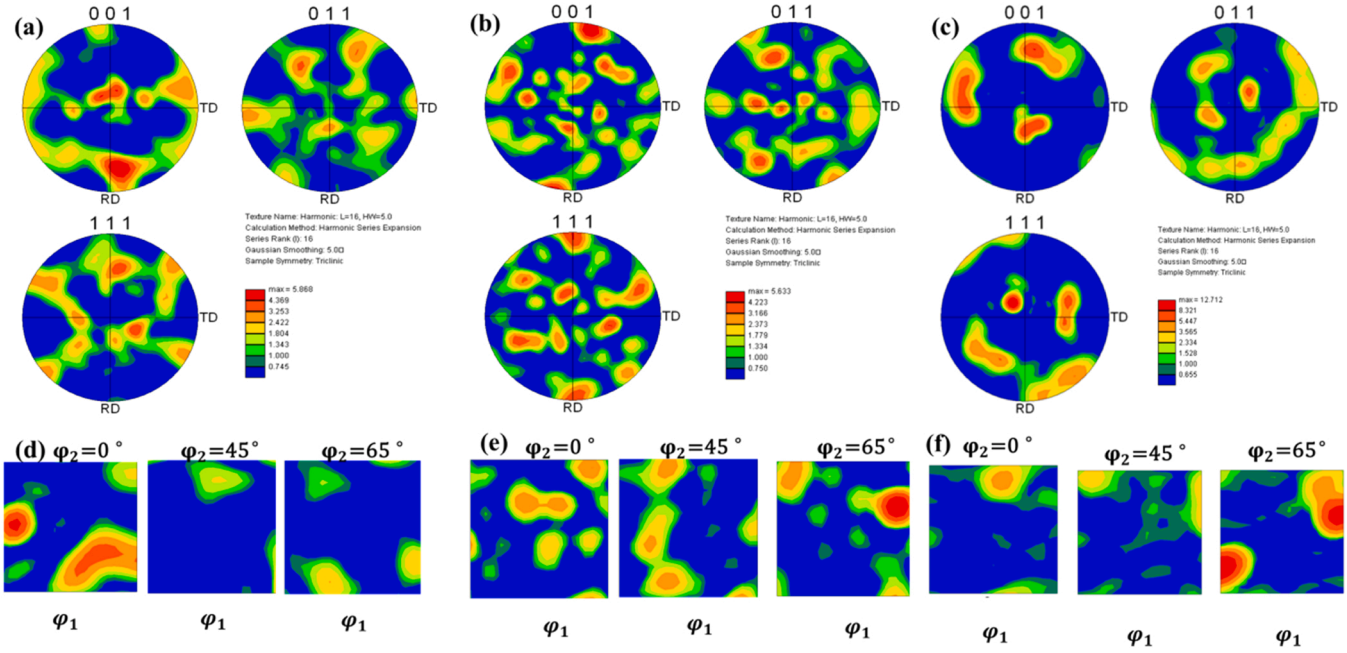

Fig. 6. Pole figures and ODF maps of Cu-1Ni-0.9Sn-0.5Ti-0.3Cr deformed at different conditions: (a), (d) 800 °C and 0.01 s^{-1} strain rate, (b), (e) 900 °C and 0.01 s^{-1} strain rate, (c), (f) 700 °C and 0.1 s^{-1} strain rate.

{011}< 211 > brass texture [58,59]. The main texture of the Cu-1Ni-0.9Sn-0.5Ti-0.3Cr alloy deformed at 0.01 s^{-1} strain rate and 800 °C is the {011}< 100 > Goss texture, based on the pole figures of the alloy in Fig. 6(a) and (b) and the ODF maps in Fig. 6(c) and (d) compared with the standard pole figures and ODF maps. For the {011}< 100 > Goss texture, the maximum strength is about 5.868. As the temperature increased from 800 °C to 900 °C, the {011}< 211 > brass texture formed instead of the {011}< 100 > Goss texture. The {011}< 211 > brass texture is the main texture, and the maximum strength decreased from 5.868 to 5.633. The number and types of textures in ODF maps of φ_2= 0, 45, and 65° sections increase when the deformation temperature increases from 800 °C to 900 °C in Fig. 6(c) and (d). This indicates that higher deformation temperature promotes dynamic recrystallization, and more recrystallized grains are generated in the alloy, which makes the texture direction more random, and the texture strength decreases. By combining the polar diagram of the alloy in Fig. 6(c) and the ODF diagram in Fig. 6(f), it can be seen that the main texture of the alloy is {112}< 111 > copper texture at 700 °C and 0.1 s^{-1} strain rate, and the maximum strength is 12.712. This indicates that the recrystallization volume fraction of the alloy is lower with fewer recrystallized grains, and the alloy has higher texture strength at lower deformation temperature and higher strain rate.

The migration of grain boundaries plays an important role in the dynamic recrystallization of alloys, and the migration of grain boundaries is related to the geometrically necessary dislocation density. The geometrically necessary dislocation density (ρ^{GND}) has the following relationship with the kernel average misorientation (KAM) obtained from EBSD [60]:

$$\rho^{GND} = 2\theta/\mu b \tag{16}$$

Here, ρ^{GND} is the geometrically necessary dislocation density in m^{-2} and θ is the mean misorientation value in radians. In this paper, the critical angle is defined as 3° and misorientation angles greater than 3° are excluded from the calculation. μ represents the step size of the scan in μm, and b is Burger's vector of 2.55 nm. Is this right, or is it 2.55 A?

Fig. 7 shows the KAM diagrams of the Cu-1Ni-0.9Sn-0.5Ti-0.3Cr alloy deformed at the strain rate of 0.01 s^{-1} at 800 °C and 900 °C, through which the geometrically necessary dislocation density ρ^{GND} can be calculated. The geometrically necessary dislocation density of the alloy at 800 °C is ρ^{GND}= 6.5 × 10^{13} m^{-2} at the strain rate of 0.01 s^{-1}, and ρ^{GND} = 4.8 × 10^{13} m^{-2} at 900 °C. Recrystallization is promoted mainly due to the temperature increases from 800 °C to 900 °C. The recrystallization process provides energy for the recrystallization by the consumption of dislocations so that the geometrically necessary dislocation density ρ^{GND} decreases with temperature. It can be calculated from KAM in Fig. 7(c) that the geometrically necessary dislocation density of the alloy is ρ^{GND} = 7.1 × 10^{13} m^{-2} at 700 °C and 0.1 s^{-1} strain

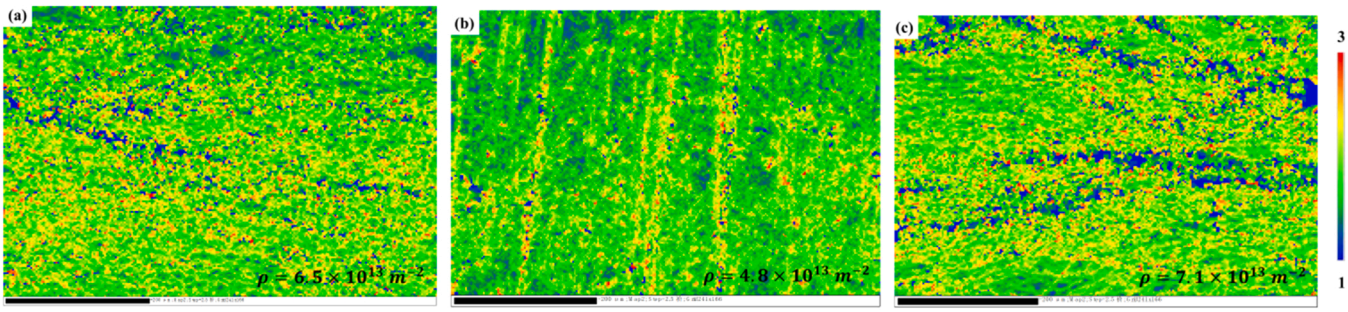

Fig. 7. The kernel average misorientation images of the Cu-1Ni-0.9Sn-0.5Ti-0.3Cr alloy deformed at: (a) 800 °C and 0.01 s^{-1} strain rate, (b) 900 °C and 0.01 s^{-1} strain rate, (c) 700 °C and 0.1 s^{-1} strain rate.

rate, and is greater than at 800 °C and 0.1 s^{-1}. This indicates that the recrystallization volume fraction of the alloy is lower with fewer recrystallized grains, the dislocation consumption is less, and the alloy has a higher dislocation density at lower deformation temperature and higher strain rate.

4.3. TEM analysis

Fig. 8 shows TEM micrographs of the Cu-1Ni-0.9Sn-0.5Ti-0.3Cr alloy deformed at 800 °C, 900 °C, and 0.01 s^{-1} strain rate. During the thermal deformation of the Cu-1Ni-0.9Sn-0.5Ti-0.3Cr alloy, crystal lattice distortions promote dislocations movement, during which dislocations entanglement and accumulation form dislocations entanglement structure, and phases precipitate near the dislocation entanglement structure, as seen in Fig. 8(a). As the deformation continues, dislocations continue to cut, accumulate, disappear and multiply, resulting in some large grains being segmented by dislocations, forming cell blocks, as seen in Fig. 8(b). When the deformation temperature rises, dislocations pile up and form dislocation packages, as seen in Fig. 8(c). Dynamic recrystallization is promoted by higher deformation temperature, forming recrystallization nuclei, neighboring grain boundaries disappear and large-angle grain boundaries are formed. The newly formed recrystallized grains grow nearby with the help of the movement of large-angle grain boundaries, as seen in Fig. 8(d). By comparing Fig. 8(b) and (d), it is found that when the deformation temperature increases from 800 ℃ to 900 ℃, the amount of precipitated phase in the alloy decreases. The precipitated phase obstructs dislocations movement, and a larger volume fraction of the precipitated phase results in a more obvious strengthening effect and higher flow stress. As the temperature increases, the amount of precipitated phase decreases, and the flow stress of the alloy decreases, which is consistent with previous results.

Fig. 9 shows the TEM microstructure of the Cu-1Ni-0.9Sn-0.5Ti-0.3Cr alloy deformed at 0.01 s^{-1} strain rate and 800 °C. In Fig. 9(a) there are many precipitated particles in the alloy. The interaction between dislocation packages and precipitated phases will hinder deformations and increase the flow stress of the alloy during hot deformation. The interaction between the precipitated phase and dislocations will also improve the deformation resistance of the alloy [61]. Fig. 9(b) is a high-resolution TEM (HRTEM) image of the precipitated phase in the white rectangle in Fig. 9(a). Fig. 9(d), and (f) are the fast Fourier transforms (FFT) of the yellow rectangle region and red rectangle region, respectively in Fig. 9(b). After FFT transformation and calibration, precipitates are determined to be the Cu and NiTi phases. The specific directions of the crystal planes of $(1\ 1\ 1)_{Cu}$ and $(1\ 1\ 0)_{NiTi}$ can be determined by the inverse FFT (IFFT) changes, as seen in Fig. 9 (b). The zone axis of the Cu phase and NiTi phase are determined to be $[\bar{1}10]_{Cu}$ and $[001]_{NiTi}$, respectively. The flow stress of the alloy during hot deformation is increased due to deformation obstruction caused by precipitation [62]. Fig. 9(c) is the geometric phase analysis (GPA) of Fig. 9(b). It is seen from the color changes that the tensile stress of most Cu phase and the compressive stress of NiTi phase are homogeneous stresses. The lattice distortions of the Cu and NiTi phases play an important role in the strengthening of the Cu-1Ni-0.9Sn-0.5Ti-0.3Cr alloy. Fig. 9(e) and (g) are the measurements of the crystal plane spacing of the $(111)_{Cu}$ and $(110)_{NiTi}$ crystal planes, and it can be concluded that $d_{(111)}$= 0.207 nm, and $d_{(110)}$= 0.224 nm. The interface between two phases can be divided into three types: coherent, semi-coherent, and non-coherent phase boundaries. The type of phase

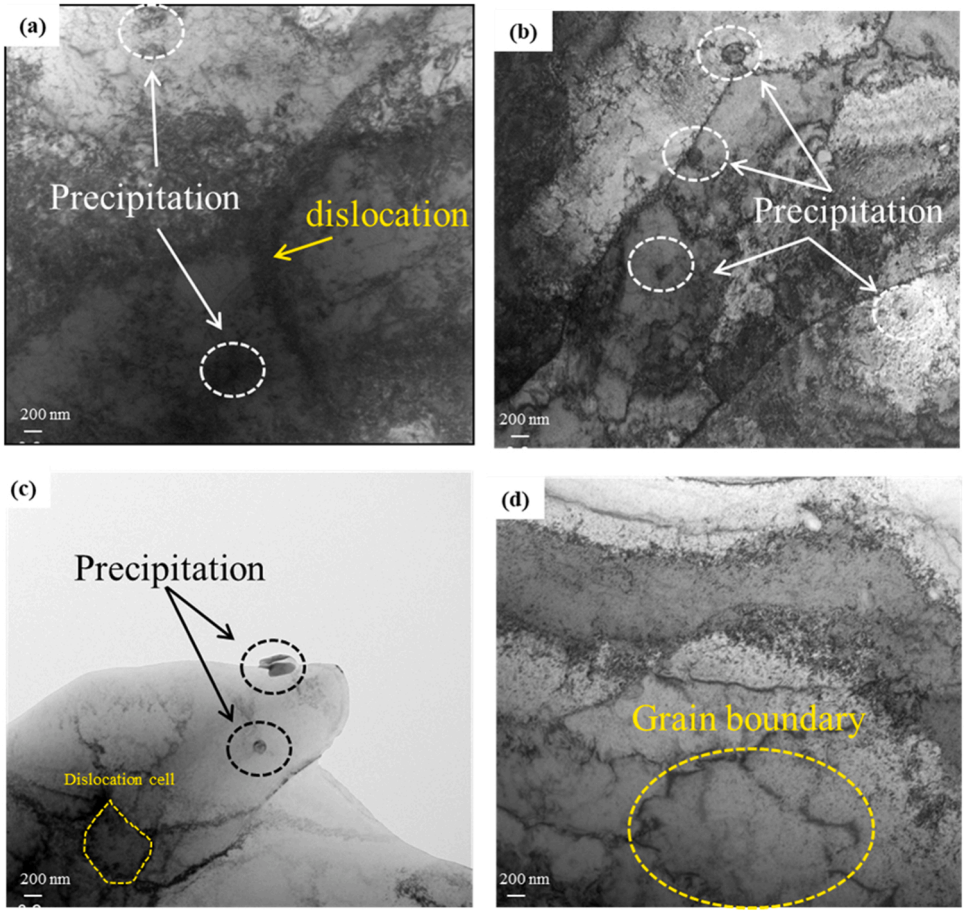

Fig. 8. TEM images of the Cu-1Ni-0.9Sn-0.5Ti-0.3Cr alloy deformed different temperatures: (a), (b) 800 ℃ and 0.01 s^{-1} strain rate, (c), (d) 900 ℃ and 0.01 s^{-1} strain rate.

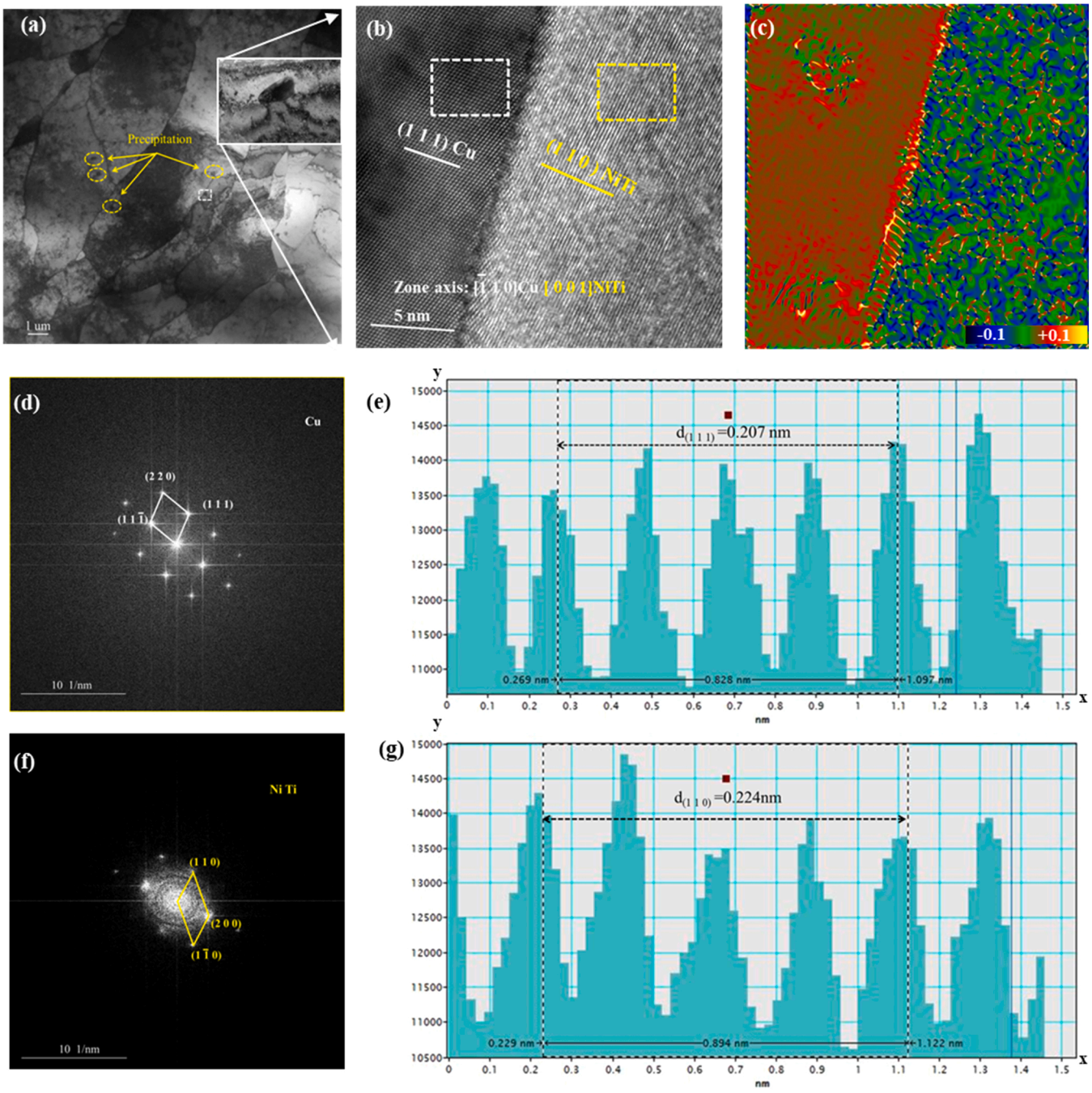

Fig. 9. TEM microstructure of Cu-1Ni-0.9Sn-0.5Ti-0.3Cr deformed at 800 °C and 0.01 s^{-1} strain rate: (a) precipitated phase, (b) HRTEM image of precipitated phase in the white rectangular frame in (a), (c) GPA map of (b), (d) and (f) FFT of the yellow rectangular frame and red rectangular frame regions in (b), respectively, (e) and (g) gray-scale spectrogram of the vertical direction of crystal plane.

boundary depends on the mismatch degree (δ) of the two matching crystal planes. If the mismatch δ< 5% the phase interface between the two phases is a coherent phase boundary. If the mismatch is 5%<δ< 15% the phase interface between the two phases is a semi-coherent phase boundary. If the mismatch degree δ> 15%, the phase interface between the two phases is a non-coherent phase boundary, and the relationship between the mismatch degree δ and the crystal plane spacing d is:

$$\delta = \frac{2\left(d_\alpha - d_\beta\right)}{d_\alpha + d_\beta} \times 100\% \tag{17}$$

Here, d_α and d_β are the plane spacing of α and β phases on both sides of the phases interface, respectively. In this experiment, Cu and NiTi phases mismatch degree is $\delta = \frac{2\left(d_\alpha - d_\beta\right)}{d_\alpha + d_\beta} = \frac{2\times(0.224-0.207)}{(0.224+0.207)} \times 100\% = 7.89\%$, Therefore, the phase interface between the Cu and NiTi phases is semi-coherent. The difference between the two Cu and TiNi lattices can be compensated by coherent deformation because the atomic distance of the coherent phase is very small. The mismatch between the two lattices of fcc Cu and bcc NiTi can be compensated for by coherent deformations since the difference in the interatomic distances of the mating phases is quite small. The precipitated phase whose phase interface between two precipitated phases is a semi-coherent interface can produce smaller elastic stress and lower interfacial energy, thus improving the refinement rate. As the resolution increases, there may be a period of time

when the lattice mismatch compensation of the two phases becomes more energetically beneficial for coherent deformation of deformed interfaces, in part because of the mismatch. With an increase in the size of precipitates, a moment can be reached when compensation for the lattice mismatch of the two phases becomes energetically more favorable not as a result of coherent deformation over the entire interface, but partially due to misfit dislocations [63]. The coherence between the two Cu and NiTi phases remains constant. Considering the degree of mismatch, the dislocation density at semi-coherent interfaces will be negligible in the intervals between which the coherence of the lattices of the two Cu and NiTi phases is observed. The precipitated phase with a high mismatch degree has high elastic stress and interface energy, and is easy to transform into the non-coherent interface, leading to the coarsening and growth of the secondary phase. The existence of the precipitated phase at the semi-coherent interface with a low mismatch degree will produce smaller elastic stress and lower interface energy, which is not conducive to the coarsening growth of the secondary phase and keeps the precipitated phase in a fine state, thus, it is beneficial to improve the refinement rate [64,65]. Given the low degree of lattice mismatch, the dislocation density at the semicoherent boundary will be negligible. Given that the Cu phase and NiTi phases are very ductile, grain refinement can effectively improve the strength and hardness of the alloy.

5. Conclusions

The Cu-1Ni-0.9Sn-0.5Ti-0.3Cr alloy used in this experiment was obtained by vacuum melting, and hot deformation tests of the Cu-1Ni-0.9Sn-0.5Ti-0.3Cr alloy were conducted under the strain rate of 0.001, 0.01, 0.1, 1, 10 s^{-1} and the temperature of 500, 600, 700, 800 and 900 °C by the Gleeble-1500 simulation device. The following conclusions could be drawn from the analysis of the experimental results:

The flow stress of the alloy increased with the decrease of temperature and the increase of strain rate during the hot deformation. The Cu-1Ni-0.9Sn-0.5Ti-0.3Cr alloy had more precipitation than pure copper, and the precipitation hindered dislocation movement, so the Cu-1Ni-0.9Sn-0.5Ti-0.3Cr alloy has higher activation energy, and the constitutive equation of its thermal deformation is:

$$\dot{\varepsilon} = e^{49.596}[\sinh(0.0071\sigma)]^{11.574} exp\left[-\frac{404150}{8.314T}\right]$$

(1) The optimal hot processing properties of the Cu-1Ni-0.9Sn-0.5Ti-0.3Cr alloy are in the 725–900 °C temperature and 0.01–0.368 s^{-1} strain rate regions. The defect-free microstructure and excellent machinability of the alloy can be obtained by hot working in this region.

(2) With the increase in deformation temperature, the average misorientation angle of EBSD of Cu-1Ni-0.9Sn-0.5Ti-0.3Cr alloy increases, and the geometric dislocation density ρ^{GND} decreases. When the deformation temperature rises from 800 °C to 900 °C, the {011}< 100 > Goss texture is replaced by the {011}< 211 > brass texture. The texture becomes more random and the maximum strength of the texture decreases from 5.868 to 5.633. Meanwhile, the recrystallization volume fraction of the alloy is lower, the number of recrystallization grains is less, and the alloy has higher texture strength at lower deformation temperature and higher strain rate.

(3) The precipitates of the Cu-1Ni-0.9Sn-0.5Ti-0.3Cr alloy are mainly the Cu and NiTi phases. The zone axes of the Cu and NiTi phases are determined to be $[\bar{1}10]_{Cu}$ and $[001]_{NiTi}$, respectively, and the interface between the two precipitates is semi-coherent. The flow stress of the alloy during hot deformation is increased due to the obstruction of deformation caused by precipitation.

CRediT authorship contribution statement

Shunlong Tang: Investigation, Experiment, Formal analysis, Writing – review & editing. **Meng Zhou:** Resources, Theoretical analysis, Formal analysis. **Xu Li:** Investigation, Formal analysis. **Yi Zhang:** Formal analysis, Writing – review & editing. **Deye Xu:** Experiment, Formal analysis. **Zhiyang Zhang:** Data curation, Formal analysis. **Baohong Tian:** Theoretical analysis, Supervision. **Yanlin Jia:** Formal analysis. **Yong Liu:** Visualization. **Alex A. Volinsky:** Writing – review & editing. **Ekaterina S. Marchenko:** Writing – review & editing.

Declaration of Competing Interest

The authors declare that they have no known competing financial interests or personal relationships that could have appeared to influence the work reported in this paper.

Acknowledgments

This work was supported by the National Natural Science Foundation of China (52071134), The Program for Innovative Research Team at the University of Henan Province (22IRTSTHN001), China Postdoctoral Science Foundation (2020M682316, 2021T140779), and Outstanding Talents Innovation Fund of the Henan Province (ZYQR201912164). AAV and ESM acknowledge support by the Mega grant from the Government of the Russian Federation No. 220 of 9 April 2010 (Agreement No. 075-15-2021–612 of 4 June 2021).

References

[1] Y.F. Geng, X. Li, Y. Zhang, Y.L. Jia, H.L. Zhou, B.H. Tian, Y. Liu, A.A. Volinsky, X. H. Zhang, K.X. Song, P. Liu, Microstructure evolution of Cu-1.0Co-0.65Si-0.1Ti alloy during hot deformation, Vacuum 177 (2020), 109376, https://doi.org/10.1016/j.vacuum.2020.109376.

[2] M. Demirtas, Microstructural, mechanical and tribological characterization of Cu-Co-Ni-Be alloy processed via equal channel angular pressing, Mater. Today Commun. 28 (2021), 102676, https://doi.org/10.1016/j.mtcomm.2021.102676.

[3] R. Markandeya, S. Nagarjuna, D.S. Sarma, Effect of prior cold work on age hardening of Cu-4Ti-1Cr alloy, Mater. Sci. Eng. A 404 (1–2) (2005) 305–313, https://doi.org/10.1016/j.msea.2005.05.072.

[4] Y.J. Ban, Y. Zhang, B.H. Tian, K.X. Song, M. Zhou, X.H. Zhang, Y.L. Jia, X. Li, Y. F. Geng, Y. Liu, A.A. Volinsky, EBSD analysis of hot deformation behavior of Cu-Ni-Co-Si-Cr alloy, Mater. Charact. 169 (2020), 110656, https://doi.org/10.1016/j.matchar.2020.110656.

[5] Y.D. Li, B.B. Yang, P. Zhang, Y. Nie, X.B. Yuan, Q. Lei, Y.P. Li, Cu-Cr-Mg alloy with both high strength and high electrical conductivity manufactured by powder metallurgy process, Mater. Today Commun. 27 (2021), 102266, https://doi.org/10.1016/j.mtcomm.2021.102266.

[6] S. Semboshi, Y. Kaneno, T. Takasugi, N. Masahashi, Suppression of discontinuous precipitation in Cu-Ti alloys by aging in a hydrogen atmosphere, Metall. Mater. Trans. A (2020) 3704–3712, https://doi.org/10.1007/s11661-020-05801-5.

[7] V. Renganathan, R. Balaji, S.M. Chen, T.W. Chen, M.A. Ali, F. Al-Hemaid, M.S. El-Shikh, Bimetallic multifunctional nanostructures based on Cu–Ni alloy for environmental sensing and catalysis applications, Vacuum 184 (2020), 109845, https://doi.org/10.1016/j.vacuum.2020.109845.

[8] J.C. Zhao, M.R. Notis, Spinodal decomposition, ordering transformation, and discontinuous precipitation in a Cu-15Ni-8Sn alloy, Acta Mater. 46 (12) (1998) 4203–4218, https://doi.org/10.1016/S1359-6454(98)00095-0.

[9] B.M. Luo, D.X. Li, C. Zhao, Z. Wang, Z.Q. Luo, W.W. Zhang, A low Sn content Cu-Ni-Sn alloy with high strength and good ductility, Mater. Sci. Eng., A 746 (2019) 154–161, https://doi.org/10.1016/j.msea.2018.12.120.

[10] Z.K. Huang, R.H. Shi, X.Y. Xiao, H.D. Fu, Q. Chen, J.X. Xie, Mechanism investigation on high-performance Cu-Cr-Ti alloy via integrated computational materials engineering, Mater. Today Commun. 27 (2021), 102378, https://doi.org/10.1016/j.mtcomm.2021.102378.

[11] S.C. Liu, J.C. Jie, J.J. Zhang, P.F. Wang, T.J. Li, G.M. Yin, A surface energy driven dissolution model for immiscible Cu-Fe alloy, J. Mol. Liq. 261 (2018) 232–238, https://doi.org/10.1016/j.molliq.2018.04.020.

[12] J.Y. Cheng, B. Shen, F.X. Yu, Precipitation in a Cu–Cr–Zr–Mg alloy during aging, Mater. Charact. 81 (2013) 68–75, https://doi.org/10.1016/j.matchar.2013.04.008.

[13] Z. Zhao, Y. Zhang, B.H. Tian, Y.L. Jia, Y. Liu, K.X. Song, Alex A. Volinsky, Co effects on Cu-Ni-Si alloys microstructure and physical properties, J. Alloy. Compd. 797 (2019) 1327–1337, https://doi.org/10.1016/j.jallcom.2019.05.135.

[14] B.J. Wang, Y. Zhang, B.H. Tian, V. Yakubov, J.C. An, Alex A. Volinsky, Y. Liu, K. X. Song, L.H. Li, M. Fu, Effects of Ce and Y addition on microstructure evolution

and precipitation of Cu-Mg alloy hot deformation, J. Alloy. Compd. 781 (2019) 118–130, https://doi.org/10.1016/j.jallcom.2018.12.022.
[15] Y.F. Geng, Y. Zhang, K.X. Song, Y.L. Jia, X. Li, H. Stock, H.L. Zhou, B.H. Tian, Y. Liu, A.A. Volinsky, X.H. Zhang, P. Liu, X.H. Chen, Effect of Ce addition on microstructure evolution and precipitation in Cu-Co-Si-Ti alloy during hot deformation, J. Alloy. Compd. 842 (2020), 155666., https://doi.org/10.1016/j.jallcom.2020.155666.
[16] H.W. Fu, J.X. Li, X.B. Yun, Role of solidification texture on hot deformation behavior of a Cu–Ni–Si alloy with columnar grains, Mater. Sci. Eng. A 824 (2021), 141862, https://doi.org/10.1016/j.msea.2021.141862.
[17] P. Zhang, Q. Lei, X.B. Yuan, X.F. Sheng, D. Jiang, Y.P. Li, Z. Li, Microstructure and mechanical properties of a Cu-Fe-Nb alloy with a high product of the strength times the elongation, Mater. Today Commun. 25 (2020), 101353, https://doi.org/10.1016/j.mtcomm.2020.101353.
[18] Y. Pang, Z. Xiao, Y.L. Jia, R. Zhang, J. Yi, W.T. Qiu, Z. Li, Hot deformation behavior of a CuAlMn shape memory alloy, J. Alloy. Compd. 845 (2020), 156161, https://doi.org/10.1016/j.jallcom.2020.156161.
[19] F. Liu, J.M. Ma, L.J. Peng, G.J. Huang, W.J. Zhang, H.F. Xie, X.J. Mi, Hot deformation behavior and microstructure evolution of Cu–Ni–Co–Si alloys, Materials 13 (2020) 2042, https://doi.org/10.3390/ma13092042.
[20] J. Liu, X.H. Wang, J. Chen, J.T. Liu, The effect of cold rolling on age hardening of Cu-3Ti-3Ni-0.5Si alloy, J. Alloy. Compd. 797 (2019) 370–379, https://doi.org/10.1016/j.jallcom.2019.05.091.
[21] Q.X. Yu, X.N. Li, K.R. Wei, Z.M. Li, Y.H. Zheng, N.J. Li, X.T. Cheng, C.Y. Wang, Q. Wang, C. Dong, Cu-Ni-Sn-Si alloys designed by cluster-plus-glue-atom model, Mater. Des. 167 (2019), 107641, https://doi.org/10.1016/j.matdes.2019.107641.
[22] Y.K. Wu, Y. Li, J.Y. Lu, S. Tan, F. Jiang, J. Sun, Correlations between microstructures and properties of Cu-Ni-Si-Cr alloy, Mater. Sci. Eng. A 731 (2018) 403–412, https://doi.org/10.1016/j.msea.2018.06.075.
[23] P. Stavroulakis, A. Toulfatzis, A. Vazdirvanidis, G. Pantazopoulos, S. Papaefthymiou. Investigation of the aging behavior of a Cu–Ni–Si rolled alloy, Metallogr, Microstruc, Springer, 2019, pp. 167–181, https://doi.org/10.1007/s13632-019-00531-6.
[24] Z. Zhao, Z. Xiao, Z. Li, W.T. Qiu, H.Y. Jiang, Q. Lei, Z.R. Liu, Y.B. Jiang, S.J. Zhang, Microstructure and properties of a Cu–Ni–Si–Co–Cr alloy with high strength and high conductivity, Mater. Sci. Eng. A 759 (2019) 396–403, https://doi.org/10.1016/j.msea.2019.05.003.
[25] J.Y. Yi, Y.L. Jia, Y.Y. Zhao, Z. Xiao, K.J. He, Q. Wang, M.P. Wang, Z. Li, Precipitation behavior of Cu-3.0Ni-0.72Si alloy, Acta Mater. 166 (2018) 261–270, https://doi.org/10.1016/j.actamat.2018.12.047.
[26] X.H. Wang, C.Y. Chen, T.T. Guo, J.T. Zou, X.H. Yang, Microstructure and properties of ternary Cu-Ti-Sn alloy, J. Mater. Eng. Perform. 24 (2015) 2738–2743, https://doi.org/10.1007/s11665-015-1483-4.
[27] J. Liu, X.H. Wang, J.T. Liu, Y.F. Liu, H.G. Li, C. Wang, Hot deformation and dynamic recrystallization behavior of Cu-3Ti-3Ni-0.5Si alloy, J. Alloy. Compd. 782 (2019) 224–234, https://doi.org/10.1016/j.jallcom.2018.12.212.
[28] K.M. Liu, Z.Y. Jiang, H.T. Zhou, D.P. Lu, A. Atrens, Y.L. Yang, Effect of heat treatment on the microstructure and properties of deformation-processed Cu-7Cr in situ composites, J. Mater. Eng. Perform. 24 (11) (2015) 4340–4345, https://doi.org/10.1007/s11665-015-1747-z.
[29] H.L. Sun, T. Zhang, A.A. Volinsky, B.J. Wang, B.J. Tian, K.X. Song, Z. Chai, Y. Liu, Effects of Ag addition on hot deformation behavior of Cu-Ni-Si alloy, Adv. Eng. Mater. 19 (2017), 1600607, https://doi.org/10.1002/adem.201600607.
[30] J.B. Correia, H.A. Davies, C.M. Sellars, Strengthening in rapidly solidified age hardened CuCr and CuCrZr alloys, Acta Mater. 45 (1997) 177–190, https://doi.org/10.1016/S1359-6454(96)00142-5.
[31] Z.Y. Dong, S.G. Jia, P.F. Zhao, M. Deng, K.X. Song, Hot deformation behavior of Cu-0.6Cr-0.03Zr alloy during compression at elevated temperatures, Mater. Sci. Eng. 570 (2013) 87–91, https://doi.org/10.1016/j.msea.2013.01.059.
[32] Z.W. Zhou, H.Y. Gong, J. You, S.B. Liu, J.L. He, Research on compression deformation behavior of aging AA6082 aluminum alloy based on strain compensation constitutive equation and PSO-BP network model, Mater. Today Commun. 28 (2021), 102507, https://doi.org/10.1016/j.mtcomm.2021.102507.
[33] T. Wei, Y.D. Wang, Z.H. Tang, S.F. Xiao, The constitutive modeling and processing map of homogenized Al-Mg-Si-Cu-Zn alloy, Mater. Today Commun. 27 (2021), 102471, https://doi.org/10.1016/j.mtcomm.2021.102471.
[34] Y.J. Ban, Y. Zhang, Y.L. Jia, B.H. Tian, A.A. Volinsky, X.H. Zhang, Q.F. Zhang, Y. F. Geng, Y. Liu, X. Li, Effects of Cr addition on the constitutive equation and precipitated phases of copper alloy during hot deformation, Mater. Des. 191 (2020), 108613, https://doi.org/10.1016/j.matdes.2020.108613.
[35] M.S. Ozerov, M.V. Klimova, N.D. Stepanov, S.V. Zherebtsov, Microstructure evolution of a TI/TIB metal-matrix composite during high-temperature deformation, Mater. Phys. Mech. 38 (2018) 54–63, https://doi.org/10.18720/MPM.3812018_8.
[36] C.M. Sellars, W.J. McTegart, On the mechanism of hot deformation, Acta Met. 14 (1966) 1136–1138, https://doi.org/10.1016/0001-6160(66)90207-0.
[37] H.D.S. Yong, S.M. Li, R.Q. Hua, Y.L. Run, L. Ping, Developed constitutive models, processing maps and microstructural evolution of Pb-Mg-10Al-0.5B alloy, Mater. Charact. 129 (2017) 353–366, https://doi.org/10.1016/j.matchar.2017.05.026.
[38] H. Mirzadeh, Quantification of the strengthening effect of reinforcements during hot deformation of aluminum-based composites, Mater. Des. 65 (2015) 80–82, https://doi.org/10.1016/j.matdes.2014.09.029.
[39] K. Edalati, Z. Horita, Correlations between hardness and atomic bond parameters of pure metals and semi-metals after processing by high-pressure torsion, Scr. Mater. 64 (2011) 161–164, https://doi.org/10.1016/j.actamat.2011.07.046.
[40] M. Ozerov, M. Klimova, V. Sokolovsky, N. Stepanov, A. Popov, M. Boldin, S. Zherebtsov, Evolution of microstructure and mechanical properties of Ti/TiB metal-matrix composite during isothermal multiaxial forging, J. Alloy. Compd. 770 (2019) 840–848, https://doi.org/10.1016/j.jallcom.2018.08.215.
[41] I. Weiss, S.L. Semiatin, Thermomechanical processing of beta titanium alloys—an overview, Mater. Sci. Eng. A 243 (1998) 46–65, https://doi/10.1016/S0921-5093(97)00783-1.
[42] V.S. Sokolovsky, N.D. Stepanov, S.V. Zherebtsov, N.A. Nochovnaya, G. A. Salishchev, Hot deformation behavior and processing maps of B and Gd containing β-solidified TiAl based alloy, Intermetallics 94 (2018) 138–151, https://doi.org/10.1016/j.intermet.2018.01.004.
[43] Y. Zhang, Z. Chai, A. Alex, B.H. Volinsky, H.L. Tian, P. Sun, Y. Liu, Liu, Processing maps for the Cu-Cr-Zr-Y alloy hot deformation behavior, Mater. Sci. Eng. A 662 (4) (2016) 320–329, https://doi.org/10.1016/j.msea.2016.03.033.
[44] H.J. McQueen, S. Yue, N.D. Ryan, E. Fry, Hot working characteristics of steels in austenitic state, J. Mater. Process. Technol. 53 (1–2) (1995) 293–310, https://doi.org/10.1016/0924-0136(95)01987-P.
[45] T. Xi, C.G. Yang, M.B. Shahzad, K. Yang, Study of the processing map and hot deformation behavior of a Cu-Bearing 317LN austenitic stainless steel, Mater. Des. 87 (2015) 303–312, https://doi.org/10.1016/j.matdes.2015.08.011.
[46] P. Zhang, C. Hu, C.G. Ding, Q. Zhu, H.Y. Qin, Platic deformation behavior and processing maps of a Ni based superalloy, Mater. Des. 65 (2015) 575–584, https://doi.org/10.1016/j.matdes.2014.09.062.
[47] I.S. Batra, G.K. Dey, U.D. Kulkarni, Microstructure and properties of a Cu-Cr-Zr alloy, J. Nucl. Mater. 299 (2) (2001) 91–100, https://doi.org/10.1016/S0022-3115(01)00691-2.
[48] I. Weiss, S.L. Semiatin, Thermomechanical processing of titanium titanium alloys—an overview, Mater. Sci. Eng. A 263 (1999) 243–256, https://doi.org/10.1016/S0921-5093(98)01155-1.
[49] S. Zherebtsov, M. Ozerov, E. Povolyaeva, V. Sokolovsky, N. Stepanov, D. Moskovskikh, G. Salishchev, Effect of hot rolling on the microstructure and mechanical properties of a Ti-15Mo/TiB Metal-Matrix composite, Metals 10 (2020) 40, https://doi.org/10.3390/met10010040.
[50] J.W. Zhao, Z.Y. Jiang, Thermomechanical processing of advanced high strength steels, Prog. Mater. Sci. 94 (2018) 174–242, https://doi.org/10.1016/j.pmatsci.2018.01.006.
[51] S. Zherebtsov, M. Ozerov, M. Klimova, D. Moskovskikh, N. Stepanov, G. Salishchev, Mechanical Behavior and Microstructure Evolution of a Ti-15Mo/TiB Titanium–Matrix Composite during Hot Deformation, Metals 9 (2019) 1175, https://doi.org/10.3390/met9111175.
[52] M. Ozerov, M. Klimova, A. Kolesnikov, N. Stepanov, S. Zherebtsov, Deformation behavior and microstructure evolution of a Ti/TiB metal-matrix composite during high-temperature compression tests, Mater. Des. 112 (2016) 17–26, https://doi.org/10.1016/j.matdes.2016.09.051.
[53] M. Subramani, Y.C. Tzeng, L.W. Tseng, Y.K. Tsai, G.S. Chen, C.Y. Chung, S. J. Huang, Hot deformation behavior and processing map of AZ61/SiC composites, Mater. Today Commun. 29 (2021), 102861, https://doi.org/10.1016/j.mtcomm.2021.102861.
[54] F. Bittner, S. Yin, A. Kauffmann, J. Freudenberger, H. Klauß, G. Korpala, R. Kawalla, W. Schillinger, L. Schultz, Dynamic recrystallization and precipitation behavior of high strength and highly conducting Cu-Ag-Zr alloys, Mater. Sci. Eng., A 597 (2014) 139–147, https://doi.org/10.1016/j.msea.2013.12.051.
[55] K.M. Liu, Z.Y. Jiang, J.W. Zhao, J. Zou, Z.B. Chen, D.P. Lu, Effect of directional solidification rate on the microstructure and properties of deformation-processed Cu-7Cr-0.1Ag in situ composites, J. Alloy. Compd. 612 (2014) 221–226, https://doi.org/10.1016/j.jallcom.2014.05.181.
[56] K. Huang, K. Marthinsen, Q.L. Zhao, R.E. Loge, The double-edge effect of second-phase particles on the recrystallization behaviour and associated mechanical properties of metallic materials, Prog. Mater. Sci. 92 (2018) 284–359, https://doi.org/10.1016/j.pmatsci.2017.10.004.
[57] Y.F. Geng, Y.J. Ban, X. Li, Y. Zhang, Y.L. Jia, B.H. Tian, M. Zhou, Y. Liu, A. A. Volinsky, K.X. Song, S.L. Tang, Excellent mechanical properties and high electrical conductivity of Cu-Co-Si-Ti alloy due to multiple strengthening, Mater. Sci. Eng., A 821 (2021), 141639, https://doi.org/10.2139/ssrn.3782845.
[58] C.S. Wang, H.D. Fu, J.X. Xie, Dynamic recrystallization behavior and microstructure evolution of high-performance Cu-3.28Ni-0.6Si-0.22Zn-0.11Cr -0.04P during hot compression, Rare Met. (2021), https://doi.org/10.1007/s12598-020-01578-z.
[59] J.W.H.G. Slakhorst, The development of recrystallization textures in F.C.C. metals with a low stacking fault energy, Acta Met. 23 (3) (1975) 301–308, https://doi.org/10.1016/0001-6160(75)90122-4.
[60] Y.S. Wu, Z. Liu, X.Z. Qin, C.S. Wang, L.Z. Zhou, Effect of initial state on hot deformation and dynamic recrystallization of Ni-Fe based alloy GH984G for steam boiler applications, J. Alloy. Compd. 795 (2019) 370–384, https://doi.org/10.1016/j.jallcom.2019.05.022.
[61] M.Y. Li, H. Wang, Y.H. Guo, H.L. Wang, D.D. Zheng, J.F. Shan, Y.Q. Chang, Microstructures and mechanical properties of the novel CuCrZrFeTiY alloy for fusion reactor, J. Nucl. Mater. 532 (2020), 152063, https://doi.org/10.1016/j.jnucmat.2020.152063.
[62] A.K. Shukla, S.V.S. Narayana Murty, S.C. Sharma, K. Mondal, Constitutive modeling of hot deformation behavior of vacuum hot pressed Cu-8Cr-4Nb alloy, Mater. Des. 75 (2015) 57–64, https://doi.org/10.1016/j.matdes.2015.03.023.

[63] S. Meher, L.J. Carroll, T.M. Pollock, M.C. Carroll, Solute partitioning in multi-component γ/γ′ Co–Ni-base superalloys with near-zero lattice misfit, Scr. Mater. 113 (2016) 185–189, https://doi.org/10.1016/j.scriptamat.2015.10.039.
[64] X.L. Zhuang, S. Antonov, L.F. Li, Q. Feng, Effect of alloying elements on the coarsening rate of γ′ precipitates in multi-component CoNi-based superalloys with high Cr content, Scr. Mater. 202 (2021), 114004, https://doi.org/10.1016/j.scriptamat.2021.114004.
[65] S. Meher, M.C. Carroll, T.M. Pollock, L.J. Carroll, Designing nickel base alloys for microstructural stability through low γ-γ′ interfacial energy and lattice misfit, Mater. Des. 140 (2018) 249–256, https://doi.org/10.1016/j.matdes.2017.11.065.